MODERN ELECTRON INDUCTION LINAC'S*

Harold Davis and Raymond Scarpetti,
Los Alamos National Laboratory, Los Alamos, NM, 87545 U.S.A.

Abstract

We describe the operating principles and history of electron induction LINAC's. Some examples of extant accelerators from around the world are presented. Trends in the development of the new generation of accelerators are coverd with examples drawn from the DARHT second axis accelerator. The technology of the pulsed power drivers and cells, and beam transport physics including beam instabilities are presented. Data from recent DARHT second axis experiments and computer simulations are discussed.

BACKGROUND

The principle of operation of the induction LINAC [1,2] is shown in figure 1. The accelerator is composed of n usually identical acceleration cells with each cell imparting an energy increment, to the beam, in the absence of the beam loading, given by Faraday's law

$$e \oint \vec{E} \bullet d\vec{l} = -e \partial/\partial t \int_s \vec{B} \bullet d\vec{S}$$, where E is the electric

field integrated along the contour shown in fig. 1, and B is the magnetic field strength enclosed by the contour, and S is the cross-sectional area defined by the contour. The total beam energy is the sum of the energy kicks given to the beam by each cell.
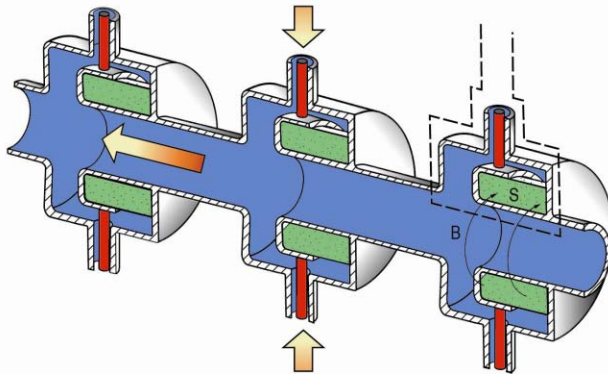

Figure 1: The induction LINAC acceleration operating principle is shown.

Each cell is driven by a high-voltage pulse forming network (PFN) with coaxial feed points distributed around the circumference of the cell. Typically, there are two to four feed points to increase azimuthal symmetry over a single feed point. In most cases, the acceleration cells contain ferromagnetic material to increase the impedance of the cell presented to the PFN (that is, the ferromagnetic material reduces the leakage current that flows from the coaxial feed around the loop surrounding the core to ground).

To avoid saturating the core material, the cross-sectional area of the core must exceed a value given by

$$S \geq \int V dt / \Delta B$$, where V is the voltage on the cell and

ΔB is the magnetic field swing of the core before saturation. Because the magnetic field swing is limited by available material properties, the required core area increases proportional to the pulse length for a given gap voltage. Some accelerators have avoided the use of magnetic material by using low-impedance radial transmission lines to drive the cell. Beam return currents flow along the wall of the beam tube through the high-voltage feeds loading the drive circuit. Thus in presence of the beam, the unloaded voltage across the acceleration gap is reduced by the product of the beam current and the internal impedance of the PFN. Most accelerators use some type of compensation network at the cell feed points to tailor the shape of the pulse. Often this is simply a shunt resistor with a resistance low enough so that the PFN is presented with an approximately resistive load.

The initial electron beam is formed in the injector. The electrons are emitted from either a thermionic cathode or a field emission cathode. Thermionic cathodes have the advantage of producing very uniform beams over a surface fixed in time. Currents up to 18 A/cm^2 can be drawn from these cathodes. These cathodes have the disadvantage that they require a very good vacuum (10^{-7} Torr or better), require water cooling, and have limited lifetime. Field emission cathodes, on the other hand, operating at the space charge limit, depend on self-produced plasma as the electron emitting surface. The plasma forms when the current drawn from sharp projections on the cathode surface rapidly ohmically heat the projections forming plasma that quickly covers the surface of the cathode. Surprisingly, ordinary velvet material has become the most commonly used material because of its low emission threshold electric field (< 50 kV/cm). Field emission cathodes can produce considerably higher current density than thermionic cathodes. For example, the DARHT first axis cathode generates about 100 A/cm^2. Field emission cathodes are very convenient to use because they are entirely passive, but have more non-uniform emission that thermionic cathodes and suffer from expansion of the plasma with time making the emission surface time-dependent, which is tolerable for short pulses (less than ~ 50 ns), but not for longer pulses.

Injectors have been driven by various pulse-power systems. These include: inductive cells, similar to the acceleration induction cells, but instead, they accelerate electrons from the cathode rather than accelerate the beam electrons; high-voltage transmission lines, charged by Marx generators; and Marx generators directly. The

inductive cells and transmission lines have been used on sub-microsecond accelerators with the Marx generator direct drive reserved for micro-second beams.

EXAMPLES OF INDUCTION LINAC'S

Ekdahl [3] has provided a list of 16 electron induction LINAC's with their operating parameters and applications. The first accelerator was built at the Lawrence Livermore Laboratory in 1963 by Nicholas Christofilos and his team to study the formation of electron layers to produce a so called "field reversed configuration" for magnetic fusion [4]. In the Astron concept, an electron beam injected into a solenoidal magnetic field formed a layer of electrons strong enough to reverse the direction of the initial magnetic field on the inside of the layer. Plasma loaded into such a field configuration is predicted to stable to magneto-hydrodynamic instabilities. The Aston I accelerator generated a 350 A, 4 MeV beam over 250 ns. The follow up Astron II accelerator produced at 850 A, 6 MeV beam over 300 ns.

Two examples of very-high-power accelerators are the LIA-30 accelerator at VNIEF in Russia [5] and the ATA accelerator at the Lawrence Livermore Laboratory [6]. These were the most powerful machines built. LIA-30 dating from 1989 produced 100 kA, 40 MeV beams over 20 ns corresponding to a peak power of 4 TW and 80 kJ per pulse. A series of radial pulses lines drive the 25-meter-long array of cells. It was used to produce powerful bursts of x-rays (10^4 Rads at one meter from the target) and neutrons (10^{14}/pulse). The ATA accelerator produced 10 kA, 45 MeV beams over 80 ns having considerably less peak power than the Russian accelerator, but nearly as much total energy. ATA used Ferrite loaded cells and was notable for a burst capability of ten pulses over one second. ATA was used for studies of atmospheric beam propagation and free electron lasers.

Perhaps the most prevalent use of induction LINAC's is to produce an x-ray pulse or pulses for flash x-radiography of dense dynamic objects (i.e., hydrodynamic tests). These accelerators have the capability of producing intense, highly collimated bursts of x-ray able to penetrate the hydrodynamic test object at its point of maximum density. Figure 2 shows the layout of one such machine – the DARHT first-axis accelerator. The "grandfather" of this accelerator class is the FXR machine [7] at LLNL dating from 1982. The FXR shown in figure 3 generates a3.3 kA, 17 MeV beam over 70 ns and produces a 400 Rad x-ray pulse one meter from the target and has a spot size of 1.8 mm (FWHM).

TRENDS IN MODERN INDUCTION LINAC'S

Modeling and Code Benchmarking

In recent years there have been a number of positive

INJECTOR   **ACCELERATOR**   Electron Beam (19.8 MeV, 1.9 kA, 60 ns)

3.9 MeV Injector Diode (field emission type), Pulse line driven   **Final focus**   **X-Ray Converter**   **64 Accelerating Cells**   Object   **γ-Ray Camera**
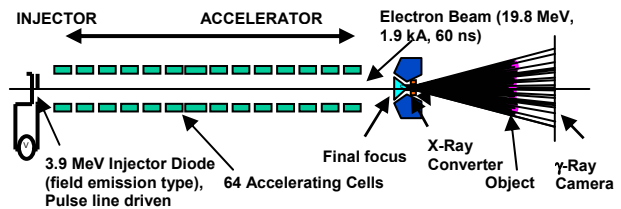
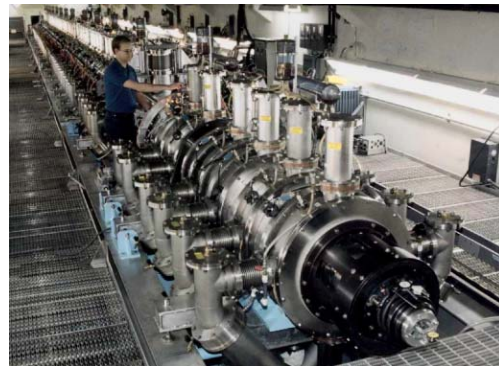Figure 2: DARHT first axis-a typical flash x-ray system.

Figure 3: The FXR accelerator at LLNL.

trends in electron induction LINAC development. First, there has been a steady improvement in computer models and the performance of the computers they run on, allowing nearly every aspect of accelerator and beam design to be computationally studied prior to assembly and testing. For example, 3-dimensional (3D), fully relativistic, electromagnetic codes are routinely used to model intrinsically 3D problems such as; beam instabilities (e.g., the beam-breakup instability or the ion-hose instability), kicker performance, and the effects of off-axis hardware. In addition, there are a number scenarios where the electron beam can come into contact with material surfaces (e.g., beam apertures, beam dumps, and x-ray conversion targets). Here, neutrals are released by thermal or stimulated desorption of impurities adsorbed on the target. These neutrals may be ionized by the beam, leading to neutralization of the beam space charge with deleterious effects on beam behavior. As an example of the value of such calculations, figure 4 shows the set-up, experimental data, and computational results from experiments that studied the effect of neutral desorption in beam target experiments [8]. In these experiments, an electron beam from the DARHT-I on
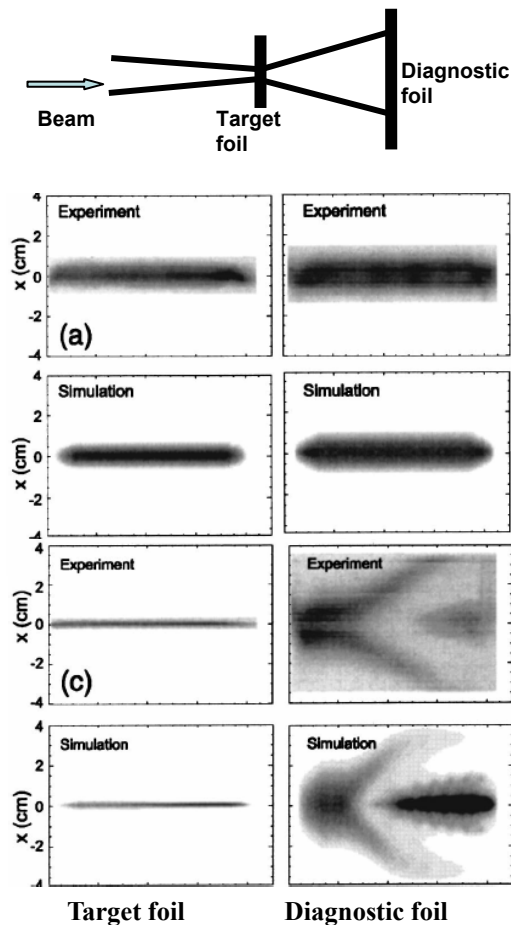
Figure 4: The top shows the layout of the two foil experiment, the center shows experiment and simulation for large beam diameter on the target foil, and the bottom shows experiment and simulation for small beam diameter on the target foil. The target foil data is on the left and the diagnostic foil data is on the right.

induction LINAC was incident on a thin foil with the size of the beam spot size varied from shot-to-shot. A second diagnostic foil was located downstream. The beam profile was monitored at this foil location with streak camera to measure the time behavior of the beam. As shown in the experimental streak photographs in fig. 4, when the beam diameter on the first foil was large, the beam diameter on both foils remained constant. However, for a sufficiently small beam spot size on the target foil, the beam is disrupted as evidenced by the rapid increase in the beam diameter on the second foil (The beam diameter on the target foil is hard to see in the photographs because of the small spot size). We strongly suspected that the disruption was due to thermal desorption of neutrals at the target foil followed by beam ionization. Three dimensional particle-in-cell (PIC) computer calculations were performed to test this hypothesis and to identify the desorbed ion species. In the calculations, the mass of the ions was varied and compared to the experimental data to get the best agreement. The computer calculations, shown in fig. 4 are

in excellent agreement with the experimental data. These calculations assume that enough neutral water molecules are released when the target undergoes a 300 C temperature rise to supply space-charge-limited ion current flow. Subsequent experiments [9] showed that the dominant desorbed species was water and that enough ions were released for space-charge-limited ion current flow.

Diagnostics

Modern induction LINAC development has also benefited from better quality and novel diagnostic devices. For example on the DARHT second axis a unique, anamorphic optical system has been used along with a set of streak cameras to view Cherenkov radiation from the beam incident on a target (see fig. 5 for sample output).[10] This allows the two-dimensional profile of the electron beam to be reconstructed as a function of time using a maximum entropy routine to unfold the data.

The light is compressed in one dimension into a line that is imaged onto a coherent, linear fiber-optic array cemented to the remotely located camera. Initially, two such arrangements provided simultaneous projections in the horizontal (X) and vertical (Y) directions, which were recorded on a 1024x1024 CCD readout camera. The system has since been extended to a four view diagnostic. The anamorphic optical system simplified alignment, eliminated ambiguity resulting from beam motion, and eased analysis. Moreover, anamorphic compression of the entire field of view in one direction simplifies the calculation of moments of the beam distribution, because the compression amounts to an optical integration in the direction orthogonal to the line image, and all that remains to be done is to compute the required moment along the direction of the line at each time.

Two other areas that modern induction LINAC's have benefited from are: better alignment tools using laser trackers, for example; and more refined pulse-power techniques used to produce more mono-energetic beams. On the DARHT second axis accelerator, improved cell alignment ($\Delta r \sim 0.25$ mm, $\Delta\theta \sim 0.2$ mr) and a highly mono-energetic beam ($\Delta E/E \sim$ +/- 0.65%, see fig. 6) has eliminated the need to tune away the effects of beam corkscrew that arises from the interaction of a non-mono-energetic beam with misaligned guide fields. This leads to a significant reduction in accelerator commissioning time.
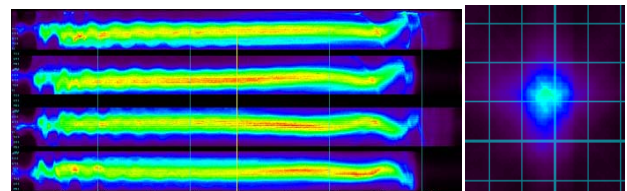

Figure 5: Top shows four streak traces from the anamorphic camera with a total sweep time of 2.3 µs and the bottom shows the reconstruction at the time indicated by the yellow line.
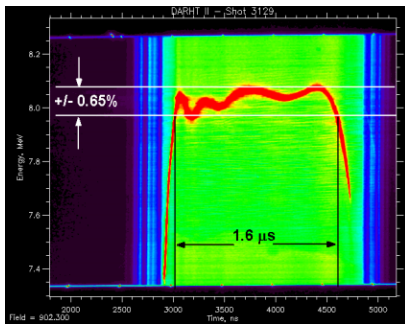
Figure 6: DARHT energy spectrometer measurement.

Table 1: DARHT Second Axis Requirements

Injector Voltage	2.5 MV
Injector Current	2.0 kilo-Amperes
Injector Pulse Length	1.6 micro-seconds
Number of Injector Cells	6 @ 175 kV/cell
Number of Accelerator Cells	68 @ 200-235 kV/cell
Total Beam Energy	17.1 MeV (goal 18.1 MeV)
Number of Pulses	4
X-ray Output	100, 100, 100, 300 Rads @ 1 meter
X-ray Spot Size (FWHM)	< 1.44 mm diameter (all pulses)

THE DARHT SECOND AXIS ACCELERATOR

DARHT Configuration

The DARHT second axis accelerator is a good illustration of modern induction LINAC technology. It is one of two accelerators used in the DARHT facility. The purpose of the DARHT facility is to benchmark and verify computer modeling of hydrodynamic experiments by providing multiple x-ray images of imploding systems along two axes.[11] DARHT consists of two induction linear accelerators oriented orthogonal to each other. Each accelerator generates a high current, 17 to 20 MeV electron beam. These electron beams converge onto bremsstrahlung targets, which convert a fraction of the electron beam kinetic energy into x-rays. Multiple x-ray pulses are then used to image the imploding device onto detectors to produce "quasi- 3 dimensional" radiographic images. The DARHT first axis has been operational since 1999 and provides a single, high-resolution radiograph. The DARHT first axis accelerator consists of a 3 MeV, 1.9 kA electron injector having a 60 ns pulse duration and 64 accelerator cells that operate at 250 kV/cell producing a final beam energy of 19 MeV.

The DARHT second axis accelerator is a 17 MeV, 2.0 kA, 1.6 µs linear induction accelerator.[12] The operational parameters of the second axis are given Table 1. The accelerator has a 2.5 MV Marx-generator-driven injector employing a 16.5-cm-diameter thermionic cathode. The beam is accelerated by 6 injector cells each operating at 175 kV and 68 accelerator cells each operating at 200 to 230 kV to produce total beam energy of 18.1 MeV.

Downstream of the accelerator, a set of dipole and quadrupole magnets deflects the beam into a beam stop below the beam line. An electromagnetic kicker is used to send portions of the beam to the target at pre-selected time intervals to produce four electron beam pulses. The four pulses are then focused onto an x-ray converter target to generate the four x-ray output pulses. The induction cell currently in operation, shown in figure 7, is an upgraded version of the original design (the upgrade is 2.54 cm longer than the original design to improve high-voltage breakdown). The acceleration cells are 1.85-m-tall, 0.53-m-long, weigh 7,300 kg each and have a bore of

35.6-cm for the injector cells and 25.4-cm for the acceleration cells (the injector cells have a large bore to accommodate the larger diameter beam near the injector).
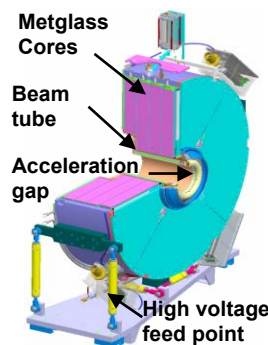

Figure 7: Cutaway drawing and photograph of the DARHT second axis cell.

The Metglas cores are located in an oil-insulated annular volume and have 480 to 520 mV-s capacity. The high-voltage vacuum insulator is made of Mycalex, which is very robust and has very good vacuum properties. The Mycalex insulator separates the oil and vacuum regions. Each cell incorporates solenoidal and x-y steering coils, and the cells are arranged in blocks of six cells. The cells are loaded in the oil region with lossy ferrites in the vicinity of the beam tube in order to damp the break-breakup instability (BBU) which is potentially a problem given the microsecond beam duration. The result is a cell design having a Q in the range of five to six. Each cell is driven by a seven-section tunable PFN in a four-stage Marx configuration. By careful tuning of the PFN's it has been possible to achieve voltage flatness over the 1.6 µs flattop of between ± 0.5-1.0 per cent, meeting the goals of the accelerator.

DARHT Second Axis Beam Prototype Tests

There are two instabilities of concern for the DARHT second axis. These are the beam breakup (BBU) instability, which was briefly mentioned earlier, and the ion hose (IH) instability. The BBU is driven by a coupling of modes in the cells with the beam transverse motion and

is well known in the accelerator community. The less familiar IH instability arises when the long pulse electron beam interacts with the residual gas in the accelerator beam tube and partially ionizes this background gas, causing an ion column. As a result, the electron beam and ion column interact causing the beam to undergo radial oscillations, spoiling the spot size at the target.

These instabilities have been addressed in a test series on the DARHT second axis using with a 1.3 kA, 7.3 MeV, 1.6-μs beam.[13] The BBU tests showed that when the instability growth rate was scaled to the current, number of cells, and the magnetic field in the final accelerator, the BBU amplitude at the output of the accelerator was less than 2% of the beam radius and less than 100 μm, indicating that BBU will not be a problem in the final accelerator configuration. Furthermore, the theoretical growth rate scaling $\Gamma \sim I \, N \, Z <1/ B_Z>$, where I is the current, N is the number of cells, Z is the transverse impedance of the cells, and $<1/ B_Z>$ is the inverse of the magnetic field averaged over the length of the accelerator was verified experimentally. When the magnetic field was lowered by an additional 68%, the BBU amplitude remained less than 5% of the beam radius indicating that there is considerable safety margin (note that $\Delta r/r <0.1$ is the requirement).

Similarly, encouraging results were obtained for the IH instability. The IH tests showed that when the instability growth rate was scaled to the final accelerator current, accelerator length, and maximum pressure (actually the machine interlock pressure), the IH amplitude at the accelerator exit was less than 2% of the beam radius. Increasing the pressure by additional factor of six produced amplitudes of $\sim$ 10% of the beam radius showing that there is a significant safety margin. As with the BBU case, the theoretical scaling of $\Gamma \sim I \, \tau \, L <p/(Ba^2)>$, where I is the beam current, τ is the beam pulse length, L is the accelerator length, and $<p/(Ba^2)>$ is the distance average of pressure normalized by the flux enclosed by the beam was confirmed.

A final set of tests are being conducted prior to assembly and commissioning of the final accelerator. These Scaled Accelerator tests maintain the same value of ν/γ as in the final accelerator. Here, ν is the Budker parameter or the number of electrons in a classical electron radius along the length of the beam and γ is the Lorentz factor. This selection preserves the relative values of the focusing and defocusing forces on the beam as in the final accelerator. In this configuration, we use the 6 injector cells of the original design at reduced voltage, and 26 of the upgraded accelerator cells operated at the design voltage of 200 to 230 kV per cell. The beam current is 960 A, the energy is 8.0 MeV, and the pulse duration is 1.6 μs. The accelerator cells have been aligned to final specifications, the cell driver PFNs, have been tuned to the required voltage "flat-top" of +/- 0.5%, and the beam energy was measured using a magnetic spectrometer to be ± 0.65% .

Initially, we have successfully completed acceleration of the beam to 8 MeV, and measured the beam emittance at the accelerator exit to be 617 π-mm-mr. More recently, we have installed the DST hardware including the kicker, beam dump, and quadrupole magnets that are used to return the beam to a circular profile after exiting the beam-dump deflector. The beam pulse duration has been reduced to 1 μs to minimize possible hardware damage in initial kicker tests. First, kicker experiments have begun with two pulses having been successfully kicked. Currently, the target assembly is being installed. After installation, kicker tests will resume with the goal of kicking four pulses. After completion of kicker work, target experiments will begin. This will complete beam tests prior to testing of the final accelerator. Installation of the remaining cells will begin in February 2007, with the commissioning of the final accelerator beginning in the spring of 2007 with a demonstration of the multi-pulse x-ray capability expected by the spring of 2008.

REFERENCES

[1] Richard J. Briggs, UCRL 99182, December 1988.

[2] Stanley Humphries, Jr., "Principles of Charged Particle Acceleration", J. Wiley, N.Y., 1986, Ch. 10.

[3] Carl Ekdahl, IEEE Trans. Plasma Sci., **30**, 1, 2002, p. 254.

[4] N. C. Christofilos, et. al., Rev. Sci. Instrum., **35**, 7, 1964, p. 886.

[5] A. I. Pavlovskii, et. al., "Linear Accelerator with Radial Lines - LIA-30", Beams 92, ed. By D. Mosher and G.. Cooperstein, p. 273.

[6] L. Reginato, IEEE Trans. Plasma Sci., **NS-30**, 4, 1983, p. 2970.

[7] Lloyd G. Multhauf, et. al., "The LLNL Flash X-ray Induction Linear Accelerator (FXR)", 25th Intl' Conf. on High-Speed Photography and Photonics, 2003.

[8] C. Vermare et. al., Phys. Plasmas, **10**, 1, 2003, p. 277.

[9] H. A. Davis, et. al., Phys. Plasmas, 10, 9. 2003, p. 3351.

[10] Carl Ekdahl et. al., IEEE Trans. Plasma Sci., **33**, 2, 2005, p. 892.

[11] M, J. Burns, et. al., 'Status of the DARHT Phase 2 Long-Pulse Accelerator', PAC 2001, p. 325.

[12] R. D. Scarpetti, et. al., "Status of the DARHT 2nd Axis at Los Alamos National Laboratory", 15th IEEE Pulsed Power Conference Proceedings, to be published Oct. 2006.

[13] Carl Ekdahl, et. al., IEEE Trans. Plasma Sci., **34**, 2, 2006, p. 460.